Title
STRANGE-PARTICLE PRODUCTION IN n+d INTERACTIONS FROM 1.1 TO 2.4 GeV/c

Authors
Davies, Donald W.
Abolins, Maris A.
Dahl, Orin I.
et al.

Publication Date
1969-12-01

Submitted to Physical Review

UCRL-19204
Preprint

c. 2

STRANGE-PARTICLE PRODUCTION IN π^+d INTERACTIONS FROM 1.1 TO 2.4 GeV/c

Donald W. Davies, Maris A. Abolins, Orin I. Dahl,
Jerome S. Danburg, Paul L. Hoch, Janos Kirz,
Donald H. Miller, and Robert K. Rader

December 1969

AEC Contract No. W-7405-eng-48

LAWRENCE RADIATION LABORATORY
UNIVERSITY of CALIFORNIA BERKELEY

STRANGE-PARTICLE PRODUCTION IN π^+d INTERACTIONS FROM 1.1 TO 2.4 GeV/c*†

Donald W. Davies,[‡] Maris A. Abolins,[**] Orin I. Dahl, Jerome S. Danburg,[††] Paul L. Hoch, Janos Kirz,[‡‡] Donald H. Miller, and Robert K. Rader

Lawrence Radiation Laboratory
University of California
Berkeley, California

ABSTRACT

We have studied properties of strange-particle final states arising from reactions of 1.1- to 2.4-GeV/c π^+ mesons on deuterium. Total cross sections on deuterium are presented and three reactions are analyzed in terms of the impulse model. $Y^*_1(1385)$ production dominates the $n\Lambda K^+\pi^+$ final state, and the reaction is described adequately near threshold by a magnetic dipole K^* exchange model. The $n\Sigma^+K^0\pi^+$ final state is found to be primarily $n\Sigma^+K^{*+}$. Highly aligned ϕ's are produced in the reaction $\pi^+d \to ppK^+K^-$, along with $\Lambda(1520)$.

Greek "phi"

"Lambda"

I. INTRODUCTION

In this paper we present results of an investigation of strange-particle production in π^+d interactions between 1.1 and 2.4 GeV/c. The experimental data come from an exposure of 250 000 pictures in the Lawrence Radiation Laboratory 72-in. deuterium-filled bubble chamber; the exposure was obtained primarily to study ω, η and η' production. The analysis of ω and η production is reported elsewhere.[1]

We first present the procedures for analyzing the data, then the cross sections for the reactions on a deuteron, comparing these to the corresponding reactions on a free nucleon. This is followed by an analysis of three final states in terms of reactions with one of the individual nucleons.

Most of the strange-particle states arising from the reaction of a positive pion with a neutron in the deuteron have been analyzed in the charge-symmetric π^-p reaction with better statistics. (See Refs. 2 and 3 and papers quoted therein.) An exception is $\pi^+n \rightarrow pK^+K^-$; this is one of the reactions considered in this report. Since the reactions on a proton have not been studied with statistics comparable to ours, we also present data on $\pi^+p \rightarrow \Lambda K^+\pi^+$ and $\pi^+p \rightarrow \Sigma^+K^0\pi^+$.

cap "sigma"

omega "eta" prime

II. EXPERIMENTAL PROCEDURES

A. Exposure size

Pictures were taken at eight different beam momenta, spaced fairly uniformly between 1.1 and 2.4 GeV/c. To determine the exposure size at each different beam momentum a special scan was made to determine the total length of beam track and the total number of interactions. The track-length determination directly gives the exposure size in events/microbarn (26.3×10^{6} cm of track gives 1 event/microbarn), and by comparing the total number of interactions with the known $\pi^{+}d$ cross section,[4] we get another determination of the events/microbarn. The two methods gave consistent results and the average was used as the exposure size (Table I).

B. Scanning and measuring procedure

The entire exposure was scanned twice for events with a visible neutral decay (vee). A list was made of all events on which the two scans disagreed as to the existence of an event or its event-type; these events were looked at again to resolve the conflict.

Assuming independent probabilities for the two scans, we find that the combined scanning efficiency on events which pass our fiducial volume cuts is 99% or greater. The assumption of independent probabilities for the two scans is not neccessarily correct; some events might be inherently less visible than others, e.g., vees with the decay plane at a small angle to the camera axis. Losses due to these effects were investigated and found to be negligible in all but the two cases discussed in the following section—short tracks on vees and Σ^+ decays—and for these two cases the remaining events were weighted to account for the loss.

The events were measured and fed into the standard Lawrence Radiation Laboratory Group A three-dimensional reconstruction and kinematic fitting program SIOUX. Events which failed to get an acceptable fit on the first measurement were remeasured once (and twice if necessary). After the event had failed three times it was looked at carefully on the scan table and the reason for failure ascertained.

C. Detection corrections

If a K^o or a Λ is produced near the bubble chamber walls there is a chance it will decay outside the visible region and be lost. Furthermore if it decays too close to the production vertex it will appear to be a non-vee event and also be lost. In order to account for losses due to these effects, fiducial volume restrictions were imposed on the events. Events which had a vee near one of the walls were flagged and treated as if they had never been found. It was determined that events with decay vertices closer than 6 mm to the production vertex also were missed. Therefore all events with neutral decay lengths less than 6 mm were also flagged and treated as if never found.

When a Λ of laboratory momentum 120 MeV/c decays with the proton going backward in the Λ rest frame, the proton is at rest in the laboratory frame. Also if the Λ has very low momentum in the laboratory frame, the vee will have a very large opening angle and will be mistaken for a stray track. We therefore have a loss of low-momentum Λ's. If the Λ has 800 MeV/c momentum and the π^- goes backward a similar situation occurs — the π^- has very low momentum and interacts or decays before going very far. Figure 1(a) shows this effect. The loss of events was parameterized by the function shown in Fig. 1(b).

The Σ^+'s produced in this experiment typically have over 1 GeV/c laboratory momentum. If the Σ^+ decays into $p\pi^o$ the proton makes a small angle with respect to the Σ^+ line of flight (<15°) and produces little change in ionization density. Under these circumstances the scanners have difficulty identifying the event as a charged decay rather than a proton scattering. Therefore, for purposes of cross-section calculation, we have used only the $n\pi^+$ decay mode of the Σ^+ and corrected the number of events to account for the $p\pi^o$ mode. The $n\pi^+$ events were also weighted to try to account for low-momentum π^+'s (as in Λ decay) and scanning losses for high-momentum collinear decays. The correction for these latter two effects was taken as 30%. Because of uncertainties in this procedure there could be systematic errors of the order of 20 o/o in the cross sections for final states containing Σ^+'s.

The events which passed the fiducial volume tests were weighted to account for these losses.

D. Separation of hypotheses

For each hypothesis that had an acceptable fit, an empirical "badness" quantity was calculated,

$$B = \chi^2{}_k - 5\ N_k + 1/2(\chi^2{}_I - N_I) - F_{kL},$$

where $\chi^2{}_k$ is the kinematic chisquared, N_k is the number of kinematic constraints, $\chi^2{}_I$ and N_I are the same for the track ionization density, and $F_{kL} = 0$ for a Λ, or $F_{kL} = 10$ for a K_S. Approximately one-third of the events had passing measurements on the Spiral Reader measuring machine, and therefore had ionization information. [See Ref. (5) for a description of the ionization routine.]

Because of the decay kinematics it is possible for most Λ's to pass as K_S's, but very few K_S decays can fake a Λ. (Because of the higher Q-value for K_S decay, the K_S usually have a much larger opening angle in the laboratory frame than a Λ). Therefore we chose to bias against the K_S fits; a factor of 10 added to the "badness" of the K_S fit was found to produce essentially perfect Λ-K_S separation.

The hypothesis with the lowest badness was tentatively accepted as the "best" fit. If there was any other hypothesis which had a badness within 10 of the best fit, and if it was possible to distinguish between the two hypotheses on the basis of track ionization, the event was looked at on the scan table. Any hypotheses which were inconsistent with the observed ionization were deleted.

III. ANALYSIS AND RESULTS

A. Cross sections

It is not necessary (or even possible in some cases) to do a separation on an event-by-event basis to get the cross section; all that is required is the number of events that should be assigned to each hypothesis. The cross sections were determined in the following way: Final states with the same visible particles were lumped together (e.g., [$n\Lambda K^+\pi^+$ and $n\Sigma^0K^+\pi^+$] or [$p\Lambda K^+$, $p\Sigma^0K^+$, $p\Lambda K^+\pi^0$, and $p\Sigma^0K^+\pi^0$], etc.). Mass and angular distributions for these events were then examined to determine how many ambiguous events to assign to each final state. Two examples will serve as illustrations:

(i) Many of the final states in this experiment are one-constraint fits (one missing non-decaying neutral) with a decaying Λ. The corresponding missing-mass (zero-constraint) hypothesis is the same final state with the Λ replaced by a Σ^0, which means that we are now missing the original neutral plus a γ ray will have a perfectly acceptable one-constraint fit, making it impossible to tell the two hypotheses apart. Therefore to get the correct number of one-and zero-constraint events, the missing-mass distributions for events with a best fit to either the one-constraint or the zero-constraint hypothesis were plotted together and the number of one-constraint events estimated. See Fig. 2 for an example of this procedure.

(ii) The states $p\Lambda K^+$ (four-constraint) and $p\Sigma^0K^+$ (two-constraint) were also impossible to distinguish on an event-by-event basis. When the Σ^0 decays so that the γ ray goes backwards along the line of flight of the Σ^0, the γ ray has very little laboratory momentum and energy, and it becomes difficult (because of the measurement errors) to distinguish it from no particle at all—i.e., a $p\Lambda K^+$ event. When the proton has a laboratory momentum less than about 80 MeV/c it does not go far enough

($\approx$2 mm) to leave a visible track, and this in effect adds on another 50 MeV/c or so in a random direction to the measurement error. Under these circumstances it is impossible to tell a Σ^0 with a backward-going γ ray from a Λ event. The "badness" function biases rather strongly in favor of the four-constraint fit, and therefore events with a soft γ ray will preferentially be called Λ events. Figure 3 shows the Σ^0 decay distributions for events with a "best" fit to a Σ^0 hypothesis; in the odd-prongs (events with an invisible proton), the loss of events with backward-going γ rays is especially conspicuous. This distribution was plotted for each beam momentum and used to determine how many Σ^0 events had been called Λ's.

The cross sections determined in this way are given in Table II and Figs. 4–8. Errors quoted take into account uncertainties in separating different final states; the cross sections quoted for final states containing a Σ^+ could have an additional 20% systematic error. (See Section II C.)

If we assume that the reactions we observe can be explained in terms of the π interacting with one of the nucleons, we can compare the deuterium cross section with the corresponding πN cross section.[2,3,6,7] These πN cross sections have been plotted with the πd cross sections in Figs. 4–6 and Fig. 8. No correction has been made to either cross section to account for the small ($\approx$ 3%) difference expected due to the screening of one nucleon by the other (see Ref. 8). For $\pi^+ n$ reactions (final state with a spectator proton) we have plotted the charge-symmetric $\pi^- p$ cross section; for $\pi^+ p$ reactions (final states with a spectator neutron) we have plotted the $\pi^+ p$ cross sections. The πd cross sections at a particular momentum should be an average of the πN cross section over $\approx$0.2 GeV/c centered at the same momentum. In general the πd and πN cross sections compare well.

B. $\pi^+ p \to \Lambda K^+ \pi^+$

We can use the $n\Lambda K^+\pi^+$ final state to get information on the reaction

$$\pi^+ p \to \Lambda K^+ \pi^+ .$$

Assuming the impulse model, the reaction $\pi^+ d \to n\Lambda K^+\pi^+$ can be thought of as

$$\begin{array}{l} \pi^+ p \to \Lambda K^+ \pi^+ , \\ \;\;(n) \;\to\; (n) \end{array}$$

where the neutron is a spectator. As a check on the assumptions of the spectator model we can compare the neutron laboratory momentum distribution to the prediction of one of the deuteron wave functions;[8] this is shown in Fig. 9 for events with a best fit to $n\Lambda K^+\pi^+$. In the rest of this analysis we have thrown out events with neutron momentum above 300 MeV/c and assumed that the impulse model is valid for the others (85 o/o of the total with best fits to this state). In order to reduce contamination from the $(n\gamma)$ $\Lambda K^+\pi^+$ final state the missing mass was required to satisfy $0.82\ (GeV/c^2)^2 < mm^2 < 0.98\ (GeV/c^2)^2$. Dividing the remaining data into four c.m. energy intervals, we get the $\Lambda K^+\pi^+$ Dalitz plots and mass projections shown in Figs. 10 and 11. A maximum-likelihood fit was made to the amount, mass, and width of the Y*(1385), assuming a p-wave Breit-Wigner form for the resonance. The results are given in Table II. Monte Carlo events were generated at the mean c.m. energy for each interval and the results plotted over the mass projections in Figs. 10 and 11.

The production angular distributions for events with $1.80\ (GeV/c^2)^2 < M_{\Lambda\pi}^2 < 2.02\ (GeV/c^2)^2$ are given in Fig. 12 after subtracting the appropriate amount of isotropic background. The production angle is defined as

$$\cos(\theta) = \hat{P}_{Y*} \cdot \hat{P}_T$$

in the c.m. of the Y*K system; $\mathbf{P}_T$ is the momentum vector of the target nucleon, defined as

$$\mathbf{P}_T = \mathbf{P}_{deuteron} - \mathbf{P}_{neutron} .$$

If we look for an explanation of the production distribution in terms of an s-channel description, we find that although there are many reported[9]

T = 3/2 N^* resonances in this mass region (2.0 GeV/c^2), none of them alone correctly reproduces the behaviour of the production distribution.

The lowest-mass particle with the correct quantum numbers for exchange in the t channel is the K*(890). In general the amplitude for this process is made up of three independent parts (corresponding to the three ways of coupling the $1/2^+$ nucleon, the 1^- K*, and some relative orbital angular momentum to make the $3/2^+$ Y*). However, there is a model that makes a specific prediction, the so-called ρ-photon analogy of Stodolsky and Sakurai.[10,11]

The ρ-photon analogy prediction for the differential cross section is

$$\frac{d\sigma}{d\Omega} \propto \frac{\sin^2\theta}{(t - m_{K^*}^2)^2},$$

lower case sigma, theta
cap omega
proportionality symbol

where t is the square of the four-momentum transfer, $t = (p_\pi - p_K)^2$. This is the function plotted over the production distributions in Fig. 12 (a-d). The fit is good at the lower two energies, poor at the higher ones. The failure of the model at higher energies is not unexpected, however — simple exchange models without absorption have always failed to give the correct amount of forward peaking in production distributions at higher energies. There is also the possibility of baryon exchange (Λ or Σ^0 for example) playing a small role and giving a backward peak to the production distribution, as indeed appears to be the case at slightly higher momentum.[12]

The model also makes predictions about the decay distribution of the Y*; these are most conveniently expressed in terms of the Y* spin density matrix elements. In the rest frame of the Y* we take the z axis parallel to the incoming target proton and the y axis normal to the production plane. In terms of Fig. 13,

$$\mathbf{n} = \mathbf{P}_K \times \mathbf{P}_p .$$

With this choice of coordinate system, the density matrix elements for the Y* are given in table IV and Fig. 14 for the four c.m. energy intervals. The ρ-photon analogy predictions are $\rho_{33} = 3/8$, $\mathrm{Re}(\rho_{31}) = 0$, $\mathrm{Re}(\rho_{3-1}) = \sqrt{3}/8$; these are the straight lines plotted on fig. 14.

Near threshold the Stodolsky-Sakurai ρ-photon analogy fits our data very well; this is similar to what is seen in the reaction $K^+p \to \Delta^{++}K^0$ near threshold [13] and the reaction $\pi^+p \to \Delta^{++}\pi^0$ at moderate energies,[14] reactions to which the model is also applicable. Above 2.06 GeV this model fails to explain our data.

C. $\pi^+p \to \Sigma^+K^0\pi^+$

The $n\Sigma^+K^0\pi^+$ final state allows us to analyze the reaction

$$\pi^+p \to \Sigma^+K^0\pi^+ .$$

Figure 15 shows the $\Sigma K\pi$ Dalitz plot and mass projections for all events with a best fit to $n\Sigma^+K^0\pi^+$. Note the very conspicuous K*(890). Figure 16 shows the $\Sigma K\pi$ center-of-mass energy. Although the threshold energy for $\Sigma K\pi$ is 1.82 GeV there are no events until the energy is sufficient to make a K* (around 2.05 GeV). Table V gives the amount, mass, and width of the K* in this final state. The curves plotted over the mass projections in fig. 15 were obtained from Monte Carlo events generated with the K* parameters given in table V and the center-of-mass energy distribution shown in fig. 16.

The center-of-mass production distribution for K* events $[0.72\ (\mathrm{GeV}/c^2)^2 < m^2_{K\pi} < 0.86\ (\mathrm{GeV}/c^2)^2]$ is given in fig. 17(a). All the angular distributions have been corrected for the small amount of background present in this $K\pi$ mass interval. Within the limited statistics of the data the production distribution is consistent with isotropy.

The K* decay distributions are shown in fig. 17(b,c) and the density matrix elements given in table VI. The curves plotted over the data in fig. 17(b, c) correspond to the density matrix elements of table VI.

D. $\pi^+ n \rightarrow pK^+K^-$

As well as the obvious strange-particle events with vees we were also able to obtain the ppK^+K^- final state. As another part of the experiment, all of the 4-prong events have been measured and processed; besides the non-strange-particle final states possible for this topology we also attempted to fit ppK^+K^-. Although the expected number of these events was only a very small fraction of the total of that topology ($\approx 0.1\ \%$), if both protons have enough momentum to be visible the ppK^+K^- final state is a 4-constraint fit and very hard for other final states to fake. Furthermore the measuring of all these events was done on the Spiral Reader, which provides track ionization information. Requiring the event to have a good kinematic fit to ppK^+K^- and also to have a low ionization χ^2 to this hypothesis resulted in approximately 250 ppK^+K^- candidates. These events were all looked at on the scanning table and events which were not ppK^+K^- were deleted. The end result was 150 4-constraint events with negligible contamination.

chi

Defining the spectator nucleon as the proton with the lower laboratory momentum and making a cut on spectator momentum at 300 MeV/c results in the c.m. energy distribution shown in fig. 18. Here the c.m. energy is defined as the energy in the pK^+K^- system, where p is the non spectator proton.

By comparing this c.m. energy distribution to a reaction with a known cross section, the $\pi^+ n \rightarrow pK^+K^-$ cross section can be determined.

In this case the reactions that were used were

$$\pi^+ n \rightarrow p\pi^+\pi^-$$
$$p\pi^+\pi^-\gamma$$
$$p\pi^+\pi^-\pi^0$$
$$p\pi^+\pi^- \text{ (missing mass).}$$

The sum of these four reactions should, by charge symmetry, have the same cross section as

$$\pi^- p \rightarrow n\pi^+\pi^-$$
$$\pi^+\pi^- \text{ (missing mass).}$$

The cross section for the sum of these two reactions is known from other experiments.[15] Making the same cuts in spectator momentum in the pK^+K^- final state and the four comparison states to eliminate high-momentum spectators, and dividing the c.m. energy distributions into three intervals, we get the cross sections given in table VII and fig. 19.

The pK^+K^- Dalitz plots and mass-squared projections for these three c.m. energy intervals are given in fig. 20. The ϕ (1020) is evident in the K^+K^- mass spectrum in intervals 1 and 3; there is also indication of Λ (1520) production in the pK^- mass spectrum of interval 2. Due to the small number of events it was impossible to do a fit to the fraction of ϕ and Λ (1520) in each interval; instead the number of events above background was estimated. Monte Carlo events were generated with this estimate of the fraction of resonance and plotted as the curve over the data in fig. 20. The estimated fractions are given in table VIII.

lower case "phi"

Table IX gives the cross section for production of ϕ and Λ (1520) (see also Ref. 2). Figure 21(a) shows the production distribution of ϕ events $[1.02\ (\text{GeV}/c^2)^2 < m^2_{K^+K^-} < 1.06\ (\text{GeV}/c^2)^2]$ and fig. 21(b,c) shows the decay distributions.

Table X contains the ϕ density matrix elements. The production is consistent with an isotropic distribution; even with the limited numbers of events available, however, it is clear from the decay distributions that the ϕ is produced highly aligned. The curves plotted over fig. 21 (b,c) correspond to the density matrix elements of table X. If the ϕ were produced by ρ exchange it would be highly aligned; however, simple ρ exchange without absorption predicts a decay distribution of the form $\sin^2\theta$, completely different from the observed distribution. This failure of a simple ρ-exchange model is very similar to the situation seen in production of the ω meson (which has the same quantum numbers as the ϕ), where the density matrix elements are similar to those of table X.[1]

We would like to express our appreciation to the Bevatron staff, the 72-inch bubble chamber crew, the scanning and measuring staff, the computer center staff, and many others. We are especially indebted to Wally Hendricks for his excellent coordination of the scanning and measuring of the film, and to Profs. Luis Alvarez and Frank Solmitz for their encouragement and support.

FOOTNOTES AND REFERENCES

*Work supported by U.S. Atomic Energy Commission.

†Part of this paper is from a thesis submitted by Donald W. Davies to the Graduate Division of the University of California–Berkeley, in partial fulfillment of the requirements for the degree of Doctor of Philosophy.

‡Presently at Department of Physics, University of California, Los Angeles.

**Presently at Department of Physics, Michigan State University, East Lansing, Michigan.

††Presently at Brookhaven National Laboratory, Upton, L.I., NY.

‡‡Presently at Department of Physics, State University of New York, Stony Brook, L.I., NY.

1. J. Danburg, A Study of the Reaction $\pi^+ d \rightarrow (p)p\pi^+\pi^-\pi^0$ at Incident Pion Momenta Between 1.1 and 2.4 BeV/c (Ph.D. thesis), UCRL-19275, July 1969.
2. O. I. Dahl, L. M. Hardy, R. I. Hess, J. Kirz, and D. H. Miller, Phys. Rev. 163, 1377 (1967).
3. O. I. Dahl, L. M. Hardy, R. I. Hess, J. Kirz, D. H. Miller, and J. A. Schwartz, Phys. Rev. 163, 1430 (1967).
4. A. A. Carter et al., Phys. Rev. 168, 1457 (1968).
5. J. Danburg and G. Lynch, Lawrence Radiation Laboratory Alvarez Programming Group Note No. P-160.
6. S. Dagan, Z. Ming Ma, J. W. Chapman, L. R. Fortney, and E. C. Fowler, Phys. Rev. 161, 1384 (1967).

7. H. L. Kraybill (Yale University), private communication.

8. V. Franco and R. J. Glauber, Phys. Rev. 142, 1195 (1966).

9. A. Donnachie, R. G. Kirsopp, and C. Lovelace, Phys. Letters 26B, 161 (1968).

10. L. Stodolsky and J. J. Sakurai, Phys. Rev. Letters 11, 90 (1963).

11. L. Stodolsky, Phys. Rev. 134, B1099 (1964).

12. P. Hoch (Lawrence Radiation Laboratory), private communication.

13. R. Bland, Single Pion Production in the K^+p Channel from 860 to 1360 MeV/c (Ph.D. thesis), UCRL-18131, March 1968.

14. G. Gidal, G. Borreani, D. Brown, F. Lott, Sun Yiu Fung, W. Jackson, and R. Pu, Evidence Concerning ρ Exchange in the Reactions $\pi^+p \rightarrow \pi^0\Delta^{++}$ and $\pi^+p \rightarrow \omega^0\Delta^{++}$, UCRL-18351, July 1968.

15. For the cross section in our center-of-mass energy range, see L. D. Jacobs, UCRL-16877; E. West, J. H. Boyd, A. R. Erwin, and W. D. Walker, Phys. Rev. 149, 1089 (1966); T. C. Bacon, W. J. Fickinger, D. G. Hill, H. W. K. Hopkins, D. K. Robinson, and E. O. Solant, Phys. Rev. 157, 1263 (1967); J. Alitti et al., Nuovo Cimento 29, 515 (1963); and E. Pickup, D. K. Robinson, E. O. Solant, F. Ayer, and B. A. Munit, Phys. Rev. 132, 1819 (1963).

16. J. Danburg (Lawrence Radiation Laboratory), private communication.

17. V. Franco and R. J. Glauber, Phys. Rev. 142, 1195 (1966).

18. R. J. Glauber, Phys. Rev. 100, 242 (1955).

Figure Captions

Fig. 1. (a) Scatter plot of the decay cosine of the Λ with respect to its line of flight versus the Λ laboratory momentum.

(b) Loss of events as a function of Λ laboratory momentum.

Fig. 2. Missing mass squared for events with a best fit to $n\Lambda K^+\pi^+$ or $(n\gamma)\Lambda K^+\pi^+$. The missing-mass-squared distribution for $(n\gamma)\Lambda K^+\pi^\mp$ was assumed to be of the shape given by the curve.

Fig. 3. Distribution of the γ ray in the Σ^0 rest frame with respect to the Σ^0 line of flight: (a) odd-prong events (events with an invisible proton), (b) even-prong events (events with a visible proton).

Fig. 4. Total cross section as a function of incident momentum for (a) $p\Lambda K^+$, (b) $p\Sigma^0K^+$, and (c) $p\Sigma^+K^0$ from this experiment (closed points). Open points are the corresponding cross sections from Refs. 2 and 3 and papers quoted therein.

Fig. 5. Total cross section as a function of incident momentum for (a) $p\Lambda K^+\pi^0$, (b) $p\Lambda K^0\pi^+$, and (c) $p\Sigma^0K^0\pi^+$ final states from this experiment (closed points). Open points are the corresponding cross sections from Refs. 2 and 3 and papers quoted therein.

Fig. 6. Total cross section as a function of incident momentum for (a) $n\Lambda K^+\pi^+$ and (b) $n\Sigma^+K^0\pi^+$ final states from this experiment (closed points). Open points are from Refs. 6 and 7.

Fig. 7. Total cross section as a function of incident momentum for (a) ppK_sK_L, (b) ppK_sK_s, and (c) $pnK^+\bar{K}^0$ final states.

Fig. 8. Total cross section as a function of incident momentum for (a) $p\Lambda K^+\pi^+\pi^-$ and (b) $p\Lambda K^0\pi^+\pi^0$ final states from this experiment (closed points). Open points are the corresponding cross sections from Refs. 2 and 3 and papers quoted therein.

Fig. 9. Laboratory momentum distribution of neutrons from $n\Lambda K^+\pi^+$ final state. The curve is the prediction of the Hulthén wave function.

Fig. 10. Dalitz plots and effective-mass-squared projections for $\Lambda K^+\pi^+$ from $n\Lambda K^+\pi^+$ final state. Center-of-mass energy less than 1.98 GeV and 1.98 GeV – 2.06 GeV.

Fig. 11. Dalitz plots and effective-mass-squared projections for $\Lambda K^+\pi^+$ from $n\Lambda K^+\pi^+$ final state. Center-of-mass energy 2.06 GeV – 2.16 GeV and 2.16 GeV – 2.36 GeV.

Fig. 12. Production angular distribution for $Y^*(1385)$ in the reaction $\pi^+ p \rightarrow Y^{*+} K^+$. Angle plotted is between the Y^* and the target proton in the Y^*K center of mass. (a) $E_{cm} < 1.98$, (b) $1.98 < E_{cm} < 2.06$, (c) $2.06 < E_{cm} < 2.16$, (d) $2.16 < E_{cm} < 2.36$ GeV. Curves are predictions of ρ-photon analogy of Stodolsky and Sakurai.

Fig. 13. Coordinate system used for Y^* decay distributions. $\hat{z}$: incoming nucleon direction; $\hat{y}$: normal to production plane; $\hat{x}$: $\hat{y}\times\hat{z}$

Fig. 14. Y^* density matrix elements. Straight lines are predictions of ρ-photon analogy.

Fig. 15. Dalitz plot and effective mass squared for $\Sigma^{+}K^{0}\pi^{+}$ from $n\Sigma^{+}K^{0}\pi^{+}$ final state.

Fig. 16. Center-of-mass energy for $\Sigma^{+}K^{0}\pi^{+}$ from $n\Sigma^{+}K^{0}\pi^{+}$ final state.

Fig. 17. $K^{*}(890)$ production and decay distributions. (a) production cosine. (b) decay cosine. (c) Treiman-Yang angle. The curves correspond to the density matrix elements of table VI.

Fig. 18. Center-of-mass energy for $pK^{+}K^{-}$ from $ppK^{+}K^{-}$ final state.

Fig. 19. Total cross section for $pK^{+}K^{-}$ as a function of center-of-mass energy.

Fig. 20. Dalitz plots and effective-mass-squared projections for $pK^{+}K^{-}$ from $ppK^{+}K^{-}$ final state. Center-of-mass energy intervals 1.95 GeV – 2.10 GeV, 2.10 GeV – 2.25 GeV, and 2.25 GeV – 2.40 GeV.

lower case phi

Fig. 21. Production and decay distributions for $\phi(1020)$. (a) production cosine. (b) decay cosine. (c) Treiman-Yang angle. The curves plotted over (b) and (c) correspond to the density matrix elements of table X.

Table I. Exposure size.

Beam momentum (GeV/c)	1.12	1.30	1.53	1.58	1.70	1.86	2.15	2.37
Events/ microbarn	0.43	0.43	2.53	0.46	2.91	2.90	2.93	0.93

lower case "mu"

Table II. Total cross sections (μb).

Final state	Beam momentum (GeV/c) 1.12	1.30	1.53	1.58	1.70	1.86	2.15	2.37
$p\Lambda K^+$	368 ± 55	475 ± 55	292 ± 20	248 ± 50	246 ± 20	167 ± 25	121 ± 25	101 ± 30
$p\Sigma^0K^+$	149 ± 45	178 ± 45	132 ± 18	135 ± 40	106 ± 15	152 ± 27	114 ± 25	77 ± 25
$p\Sigma^+K^0$	39 ± 39	254 ± 90	234 ± 45	270 ± 90	188 ± 39	174 ± 33	142 ± 33	52 ± 33
$p\Lambda K^+\pi^0$			79 ± 10	89 ± 22	114 ± 9	131 ± 9	151 ± 12	150 ± 22
$p\Lambda K^0\pi^+$		9 ± 7	69 ± 7	73 ± 18	84 ± 7	104 ± 8	160 ± 10	126 ± 17
$p\Sigma^0K^0\pi^+$			21 ± 11	0 ± 18	19 ± 9	34 ± 10	55 ± 15	74 ± 29
$n\Lambda K^+\pi^+$		11 ± 7	72 ± 12	65 ± 22	108 ± 12	134 ± 14	118 ± 12	67 ± 16
$n\Sigma^+K^0\pi^+$					7 ± 15	62 ± 21	110 ± 26	160 ± 60
ppK_SK_L			1.9± 1.2	0.0± 4.0	17.5± 3.5	18.6± 3.5	28.6± 4.5	18.7± 7.5
ppK_SK_S					6.2± 3.1	8.4± 3.5	13.2± 5.1	5.2± 5.2
$pnK^+\bar{K}^0$			4.0± 2.8	11 ± 11	20 ± 6	25 ± 6	48 ± 9	67 ± 18
$p\Lambda K^+\pi^+\pi^-$					10 ± 3	18 ± 4	47 ± 7	58 ± 15
$p\Lambda K^0\pi^+\pi^0$					3.3± 3.3	9.7± 5.5	28 ± 10	63 ± 24

Table III. $Y^*(1385)$ amount, mass, and width.

Center of mass energy (GeV)			Fraction	Mass (GeV/c^2)	Width (GeV/c^2)
threshold[a]	-	1.98	0.92±.08	1.3866±.0044	0.049 ±.011
1.98	-	2.06	0.80±.09	1.3850±.0031	0.045 ±.010
2.06	-	2.16	0.69±.07	1.3828±.0020	0.0255±.0046
2.16	-	2.36	0.39±.06	1.3868±.0020	0.0217±.0062

(a) We found no $n\Lambda K^+\pi^+$ events with $\Lambda K^+\pi^+$ center-of-mass energy below threshold for Y^*K production.

Table IV. Y^* density matrix elements in $\pi^+ p \rightarrow Y^{*+} K^+$.

Center-of-mass energy (GeV)	$\rho_{3,3}$	$\mathrm{Re}(\rho_{31})$	ρ_{3-1}
threshold – 1.98	0.39±.05	0.07±.05	0.17±.07
1.98 – 2.06	0.42±.05	0.02±.06	0.27±.06
2.06 – 2.16	0.12±.06	0.07±.06	0.24±.06
2.16 – 2.36	0.21±.06	-0.05±.07	0.18±.07

Table V. $K^*(890)$ parameters in $\pi^+ p \to \Sigma^+ K^{*+}$.

Fraction	Mass (GeV/c^2)	Width (GeV/c^2)
0.75±.10	0.895±.006	0.051±.017

Table VI. $K^*(890)$ density matrix elements in $\pi^+ p \to \Sigma^+ K^{*+}$.

$\rho_{0,0}$	$\rho_{1,1}$	$\rho_{1,-1}$	$\mathrm{Re}(\rho_{1,0})$
0.124±.082	0.438±.041	0.063±.074	0.097±.050

rlw

Table VII. Cross section for $\pi^+ n \rightarrow pK^+K^-$.

Center-of-mass energy (GeV)	Cross section (μb)
1.95 - 2.10	38±7
2.10 - 2.25	67±10
2.25 - 2.40	102±19

lower case "phi"

Table VIII. Fraction of $\phi(1020)$ and $\Lambda(1520)$

Center-of-mass energy (GeV)	Estimated fraction $\phi(1020)$	Estimated fraction $\Lambda(1520)$
1.95 - 2.10	0.5	0.0
2.10 - 2.25	0.1	0.3
2.25 - 2.40	0.2	0.1

Table IX. Cross sections for $\pi^+ n \rightarrow p\phi$ and $\pi^+ n \rightarrow \Lambda(1520)K^+$.

Center-of-mass energy (GeV)	Cross section (μb[redacted])	
	$\pi^+ n \rightarrow p\phi$	$\pi^+ n \rightarrow \Lambda(1520)K^+$
1.95 – 2.10	38 ± 11	0 ± 13
2.10 – 2.25	14^{+21}_{-6}	94 ± 36
2.25 – 2.40	42 ± 17	45^{+45}_{-31}

Table X. Density matrix elements for $\phi(1020)$.

$\rho_{0,0}$	$\rho_{1,1}$	$\rho_{1,-1}$	$\mathrm{Re}(\rho_{1,0})$
$0.64 \pm .14$	$0.18 \pm .07$	$-0.24 \pm .09$	$-0.25 \pm .08$

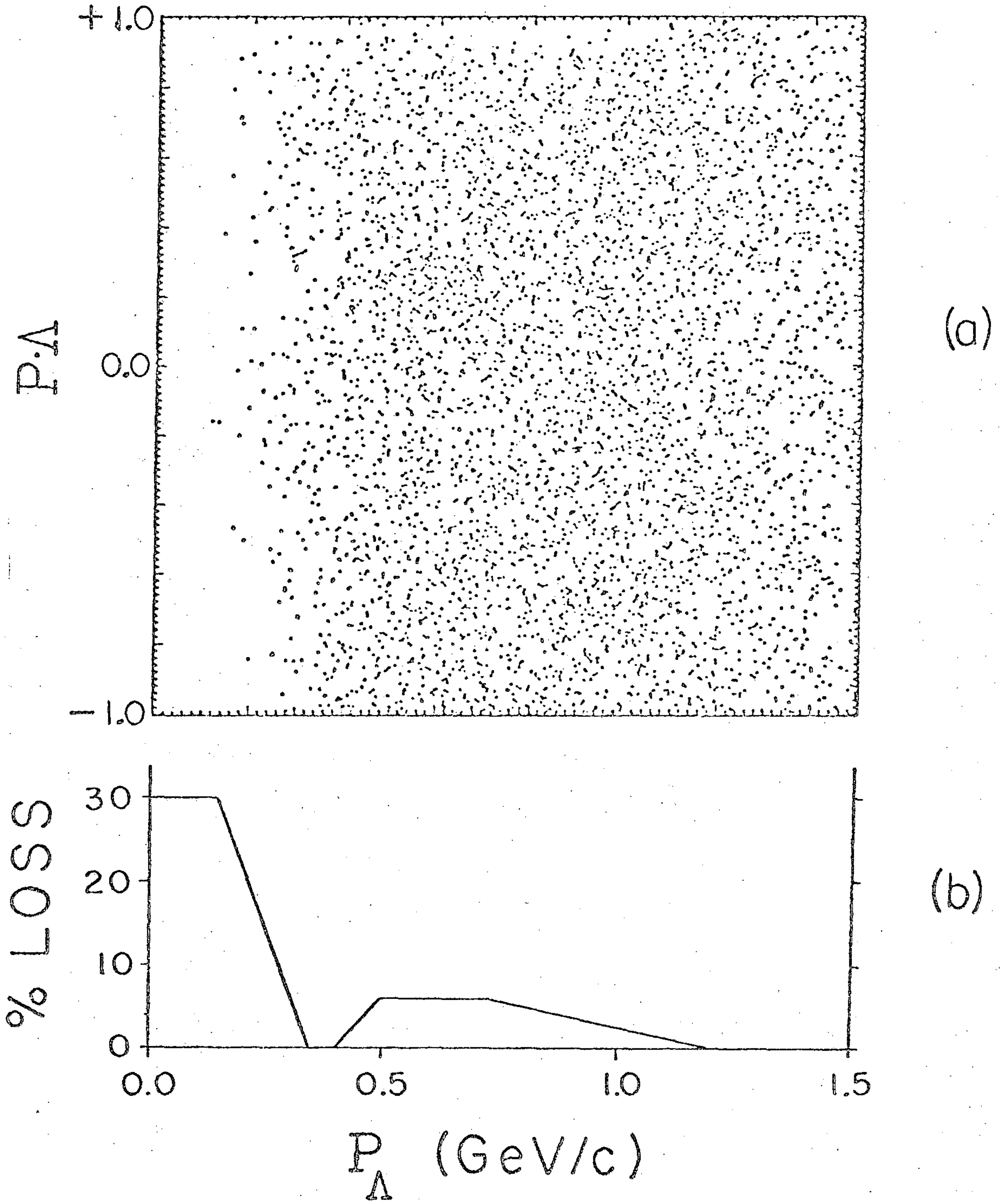

XBL 697-1056

Fig 1a, b

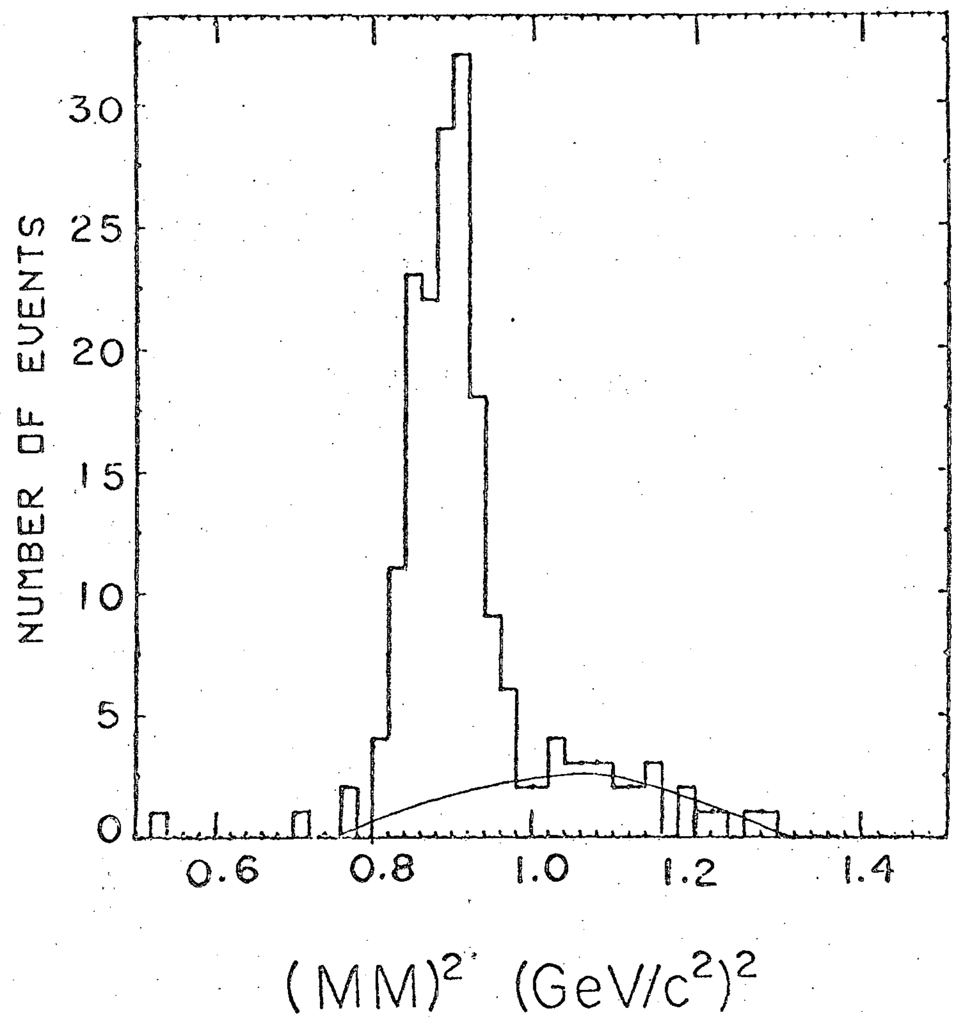

XBL 698-1101

Fig 2

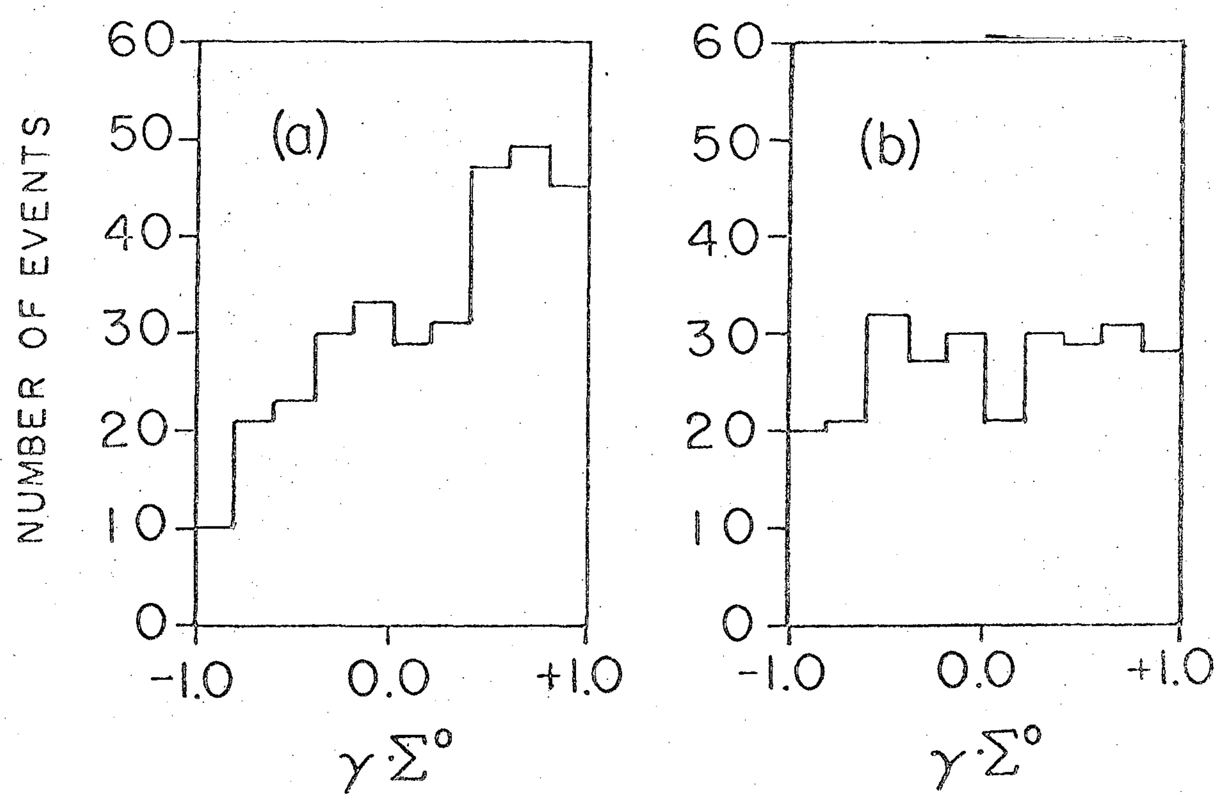

XBL 697-1057

Fig. 3a, b

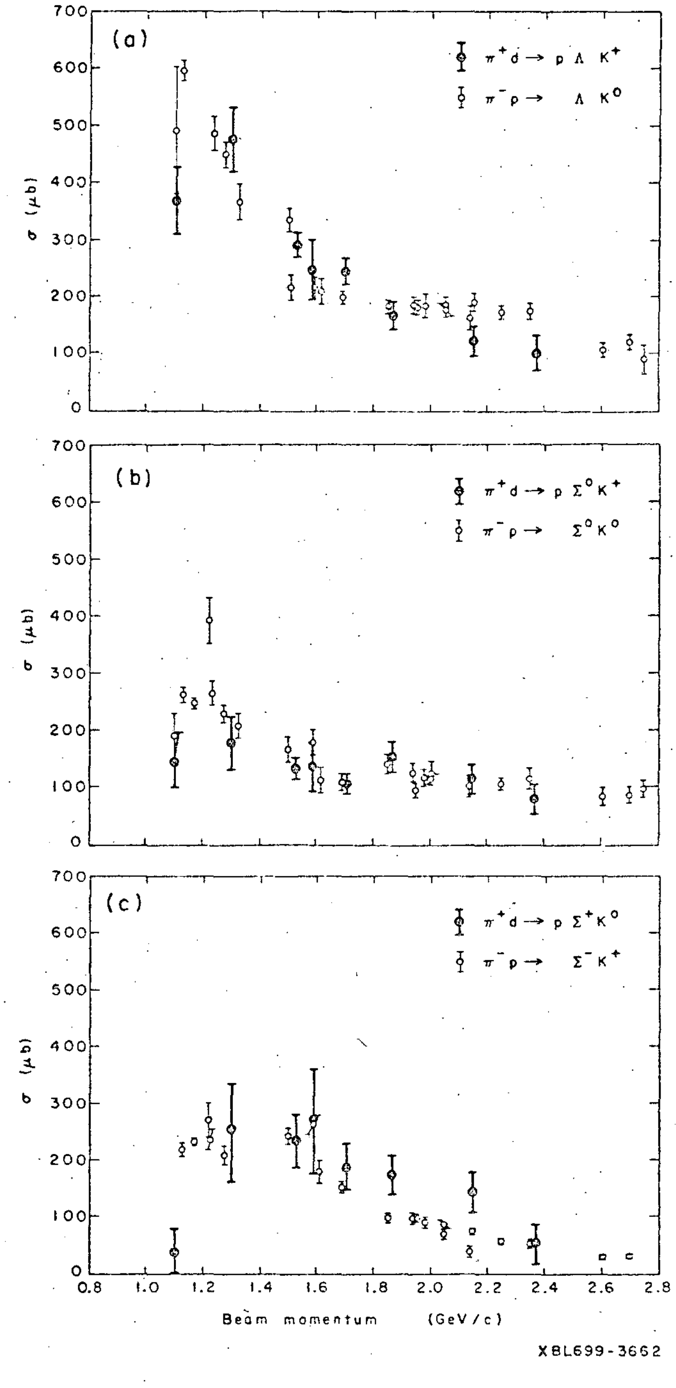

(a)
$\pi^+ d \to p \Lambda K^+$
$\pi^- p \to \Lambda K^0$
(b)
$\pi^+ d \to p \Sigma^0 K^+$
$\pi^- p \to \Sigma^0 K^0$
(c)
$\pi^+ d \to p \Sigma^+ K^0$
$\pi^- p \to \Sigma^- K^+$
σ (μb)
Beam momentum (GeV/c)
XBL699-3662

Fig 4.

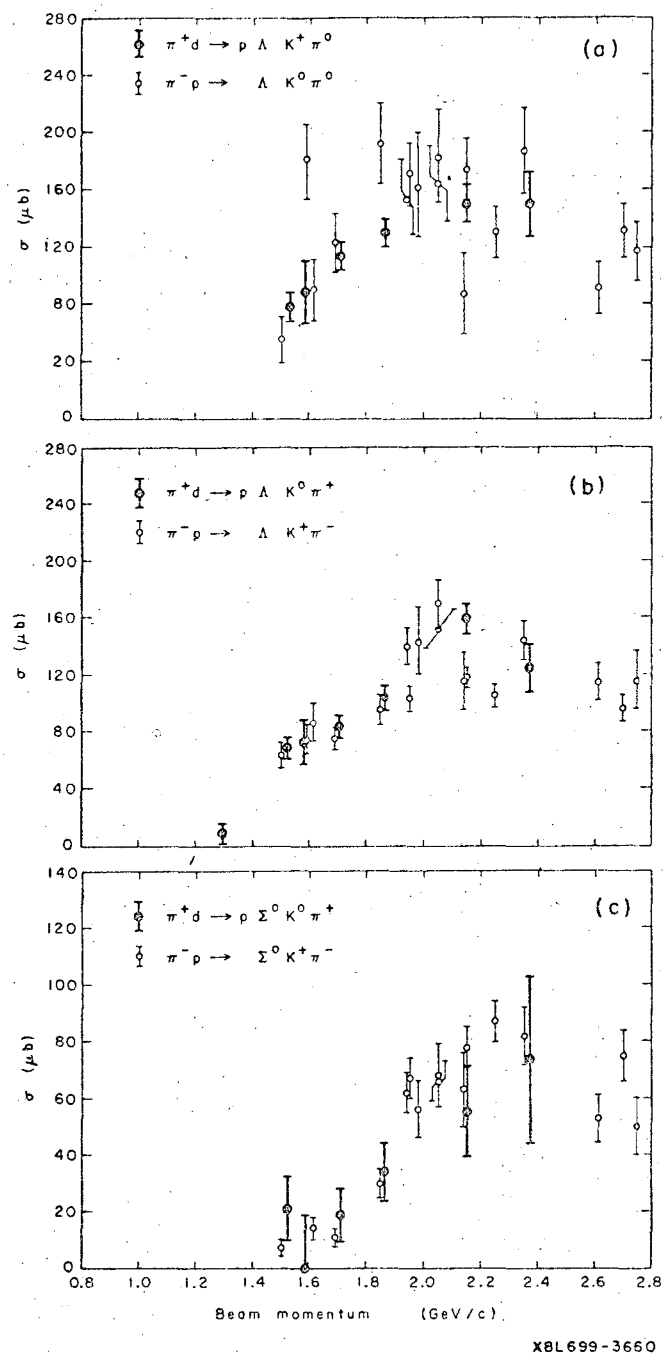

(a)
$\pi^+ d \rightarrow p \Lambda K^+ \pi^0$
$\pi^- p \rightarrow \Lambda K^0 \pi^0$
(b)
$\pi^+ d \rightarrow p \Lambda K^0 \pi^+$
$\pi^- p \rightarrow \Lambda K^+ \pi^-$
(c)
$\pi^+ d \rightarrow p \Sigma^0 K^0 \pi^+$
$\pi^- p \rightarrow \Sigma^0 K^+ \pi^-$
σ (μb)
Beam momentum (GeV/c)
XBL699-3660

Fig 5.

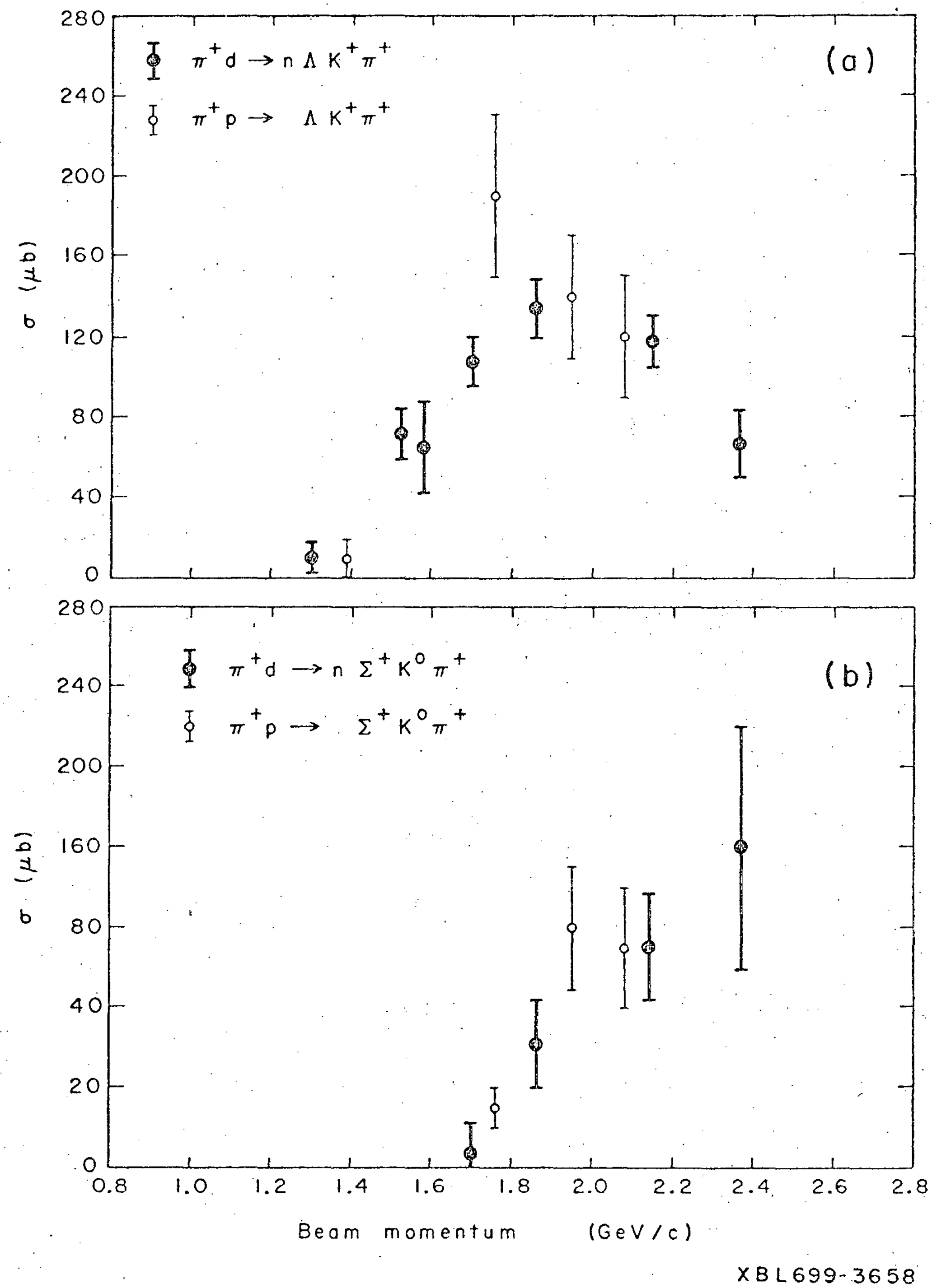

280
240
200
160
120
80
40
0
σ (μb)
$\pi^+ d \to n \Lambda K^+ \pi^+$
$\pi^+ p \to \Lambda K^+ \pi^+$
(a)
280
240
200
160
80
40
20
0
σ (μb)
$\pi^+ d \to n \Sigma^+ K^0 \pi^+$
$\pi^+ p \to \Sigma^+ K^0 \pi^+$
(b)
0.8
1.0
1.2
1.4
1.6
1.8
2.0
2.2
2.4
2.6
2.8
Beam momentum (GeV/c)
XBL699-3658

Fig 6.

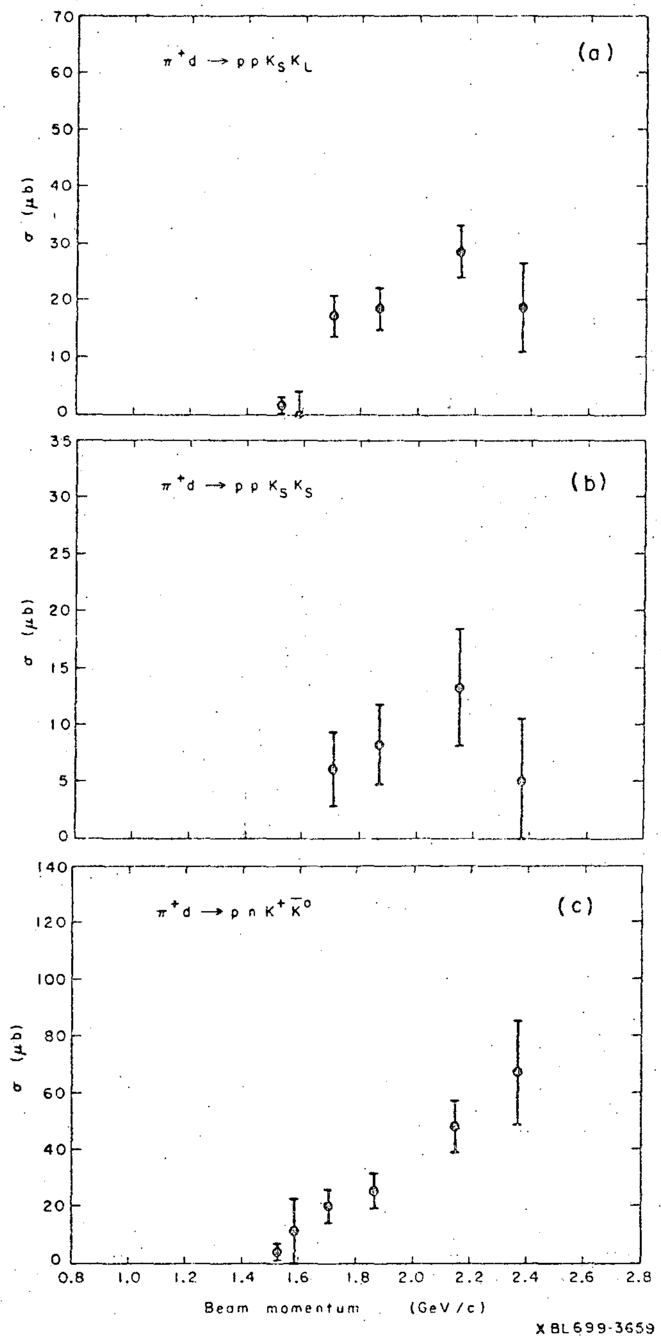

(a)
$\pi^+ d \to p p K_S K_L$
(b)
$\pi^+ d \to p p K_S K_S$
(c)
$\pi^+ d \to p n K^+ \bar{K}^0$
σ (μb)
Beam momentum (GeV/c)
XBL699-3659

Fig. 7.

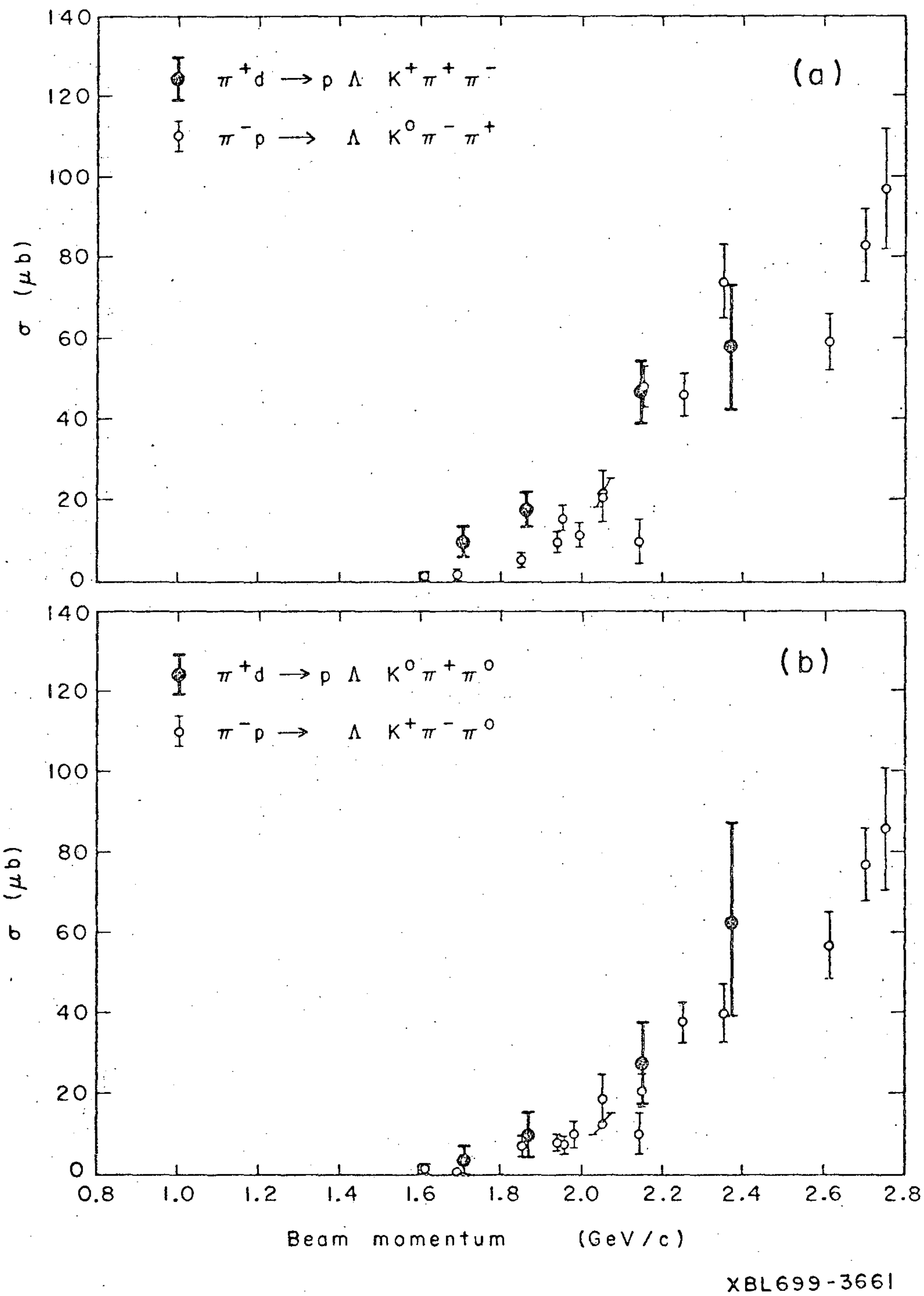

(a)
$\pi^+ d \rightarrow p \Lambda K^+ \pi^+ \pi^-$
$\pi^- p \rightarrow \Lambda K^0 \pi^- \pi^+$
(b)
$\pi^+ d \rightarrow p \Lambda K^0 \pi^+ \pi^0$
$\pi^- p \rightarrow \Lambda K^+ \pi^- \pi^0$
σ (μb)
0
20
40
60
80
100
120
140
0.8
1.0
1.2
1.4
1.6
1.8
2.0
2.2
2.4
2.6
2.8
Beam momentum (GeV/c)
XBL699-3661

Fig 8.

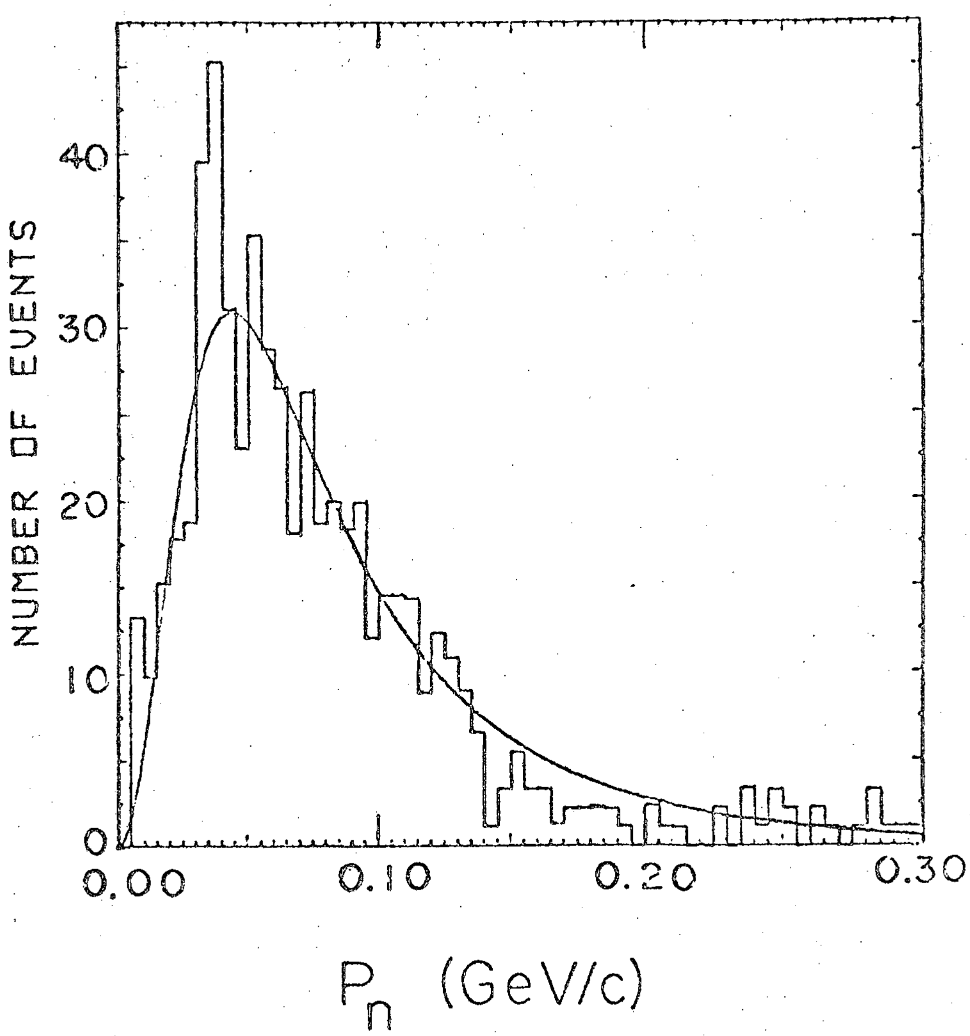

XBL 698-1154

Fig. 9.

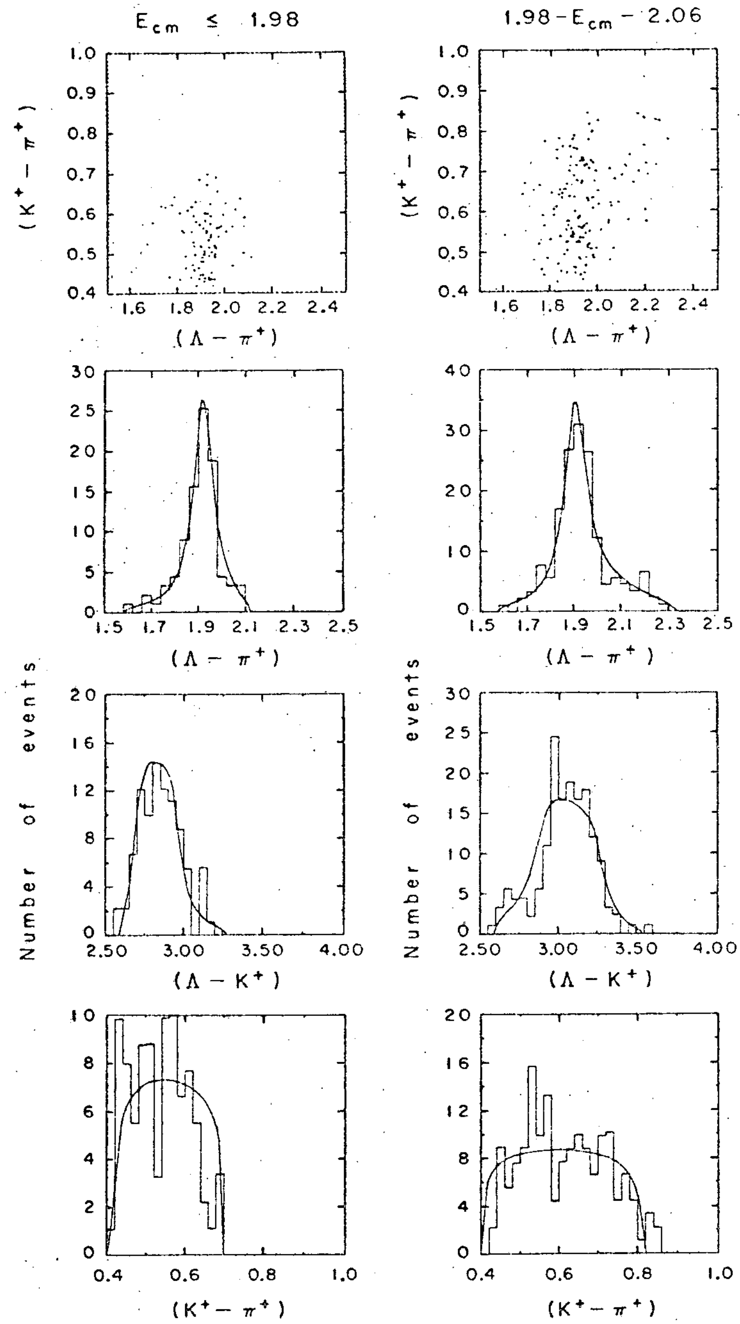

XBL 697-3160

Fig 10

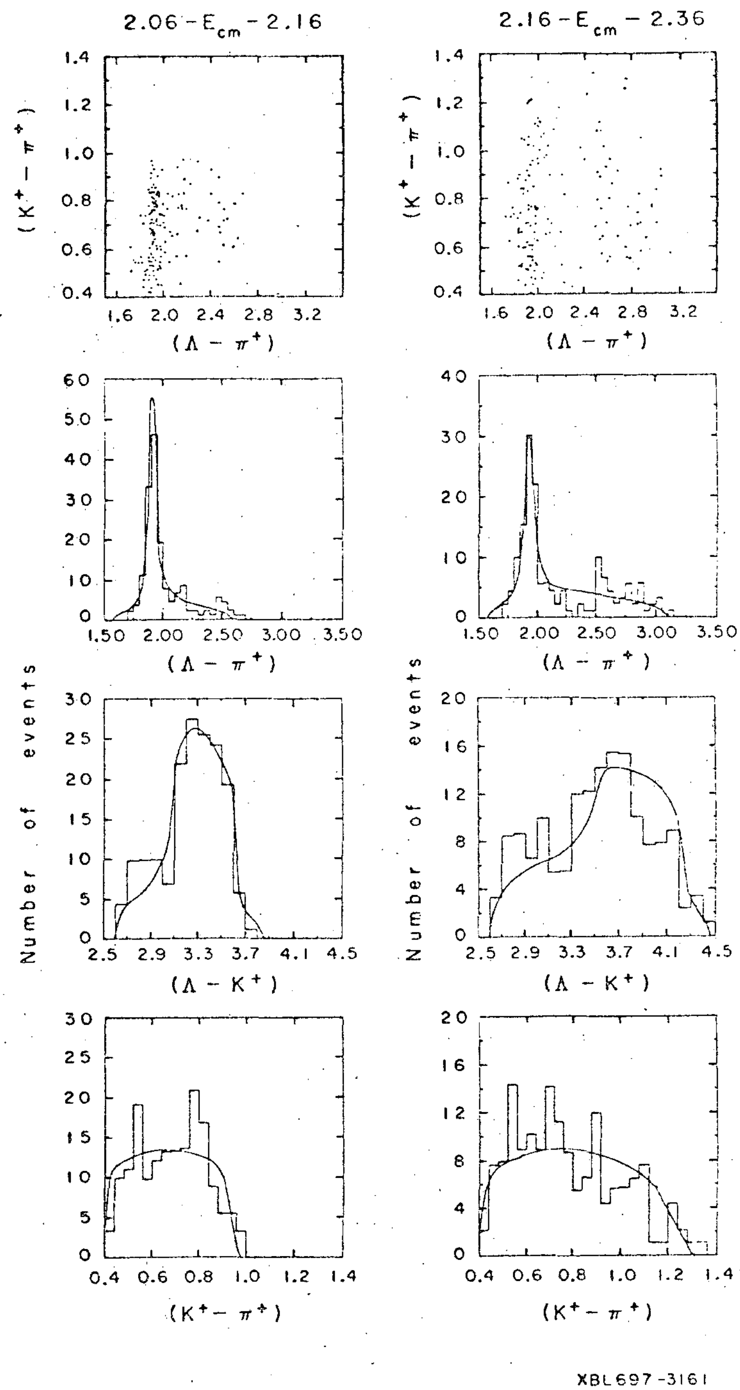
2.06 - E_{cm} - 2.16
2.16 - E_{cm} - 2.36
$(K^+ - \pi^+)$
$(\Lambda - \pi^+)$
$(\Lambda - K^+)$
Number of events
XBL697-3161

Fig 11

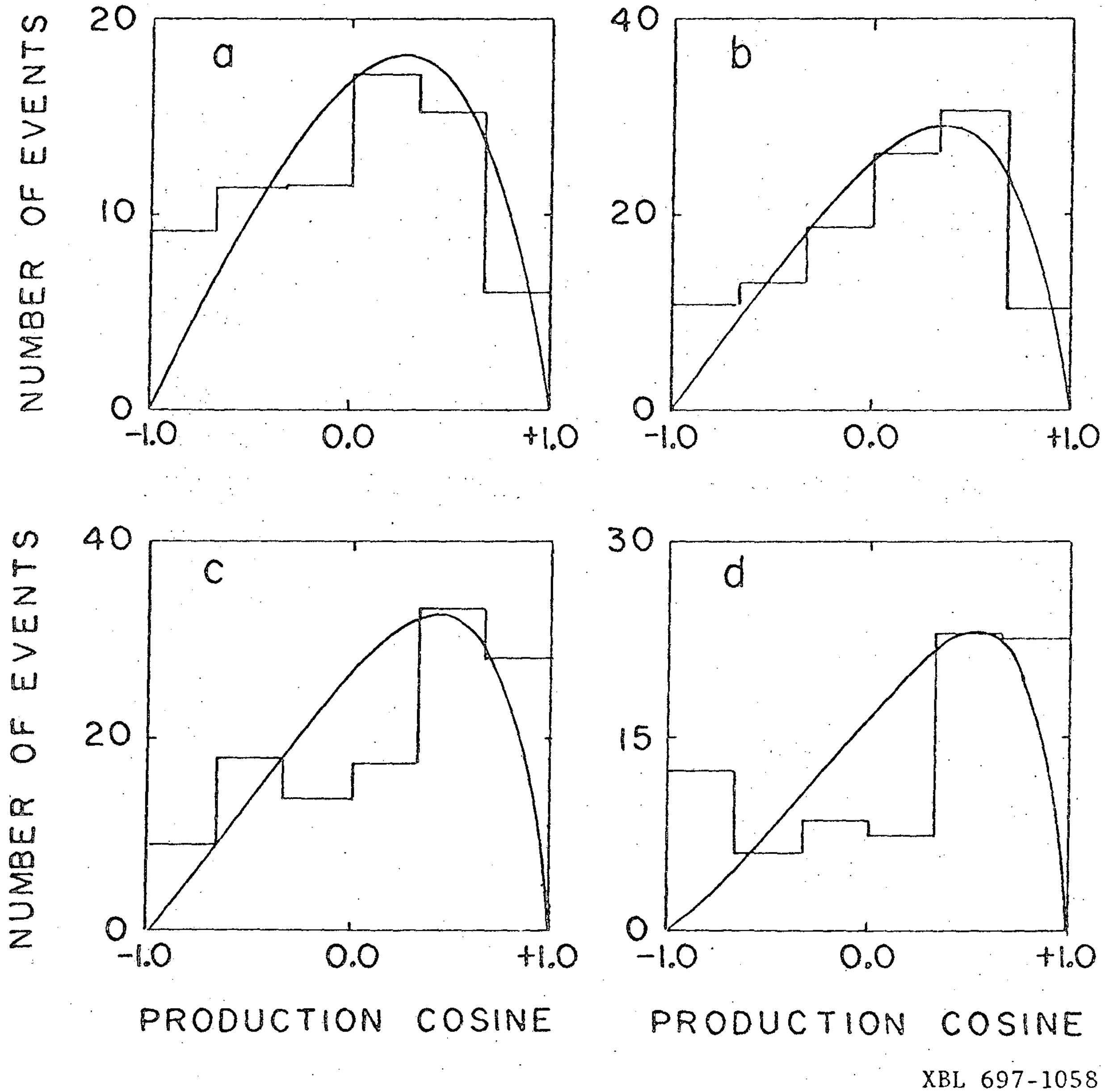
NUMBER OF EVENTS
a
b
c
d
20
10
0
40
30
15
-1.0
0.0
+1.0
PRODUCTION COSINE
XBL 697-1058

Fig 12

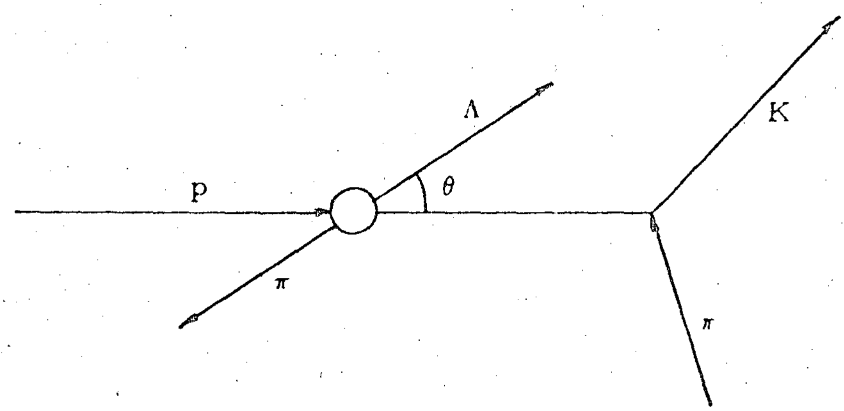

XBL 697-1059

Fig 13

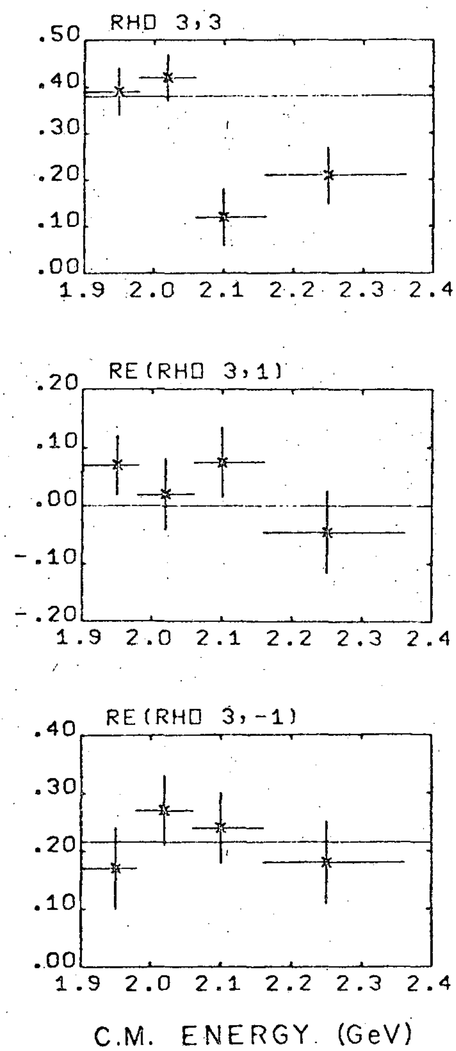

XBL 696-622

Fig 14

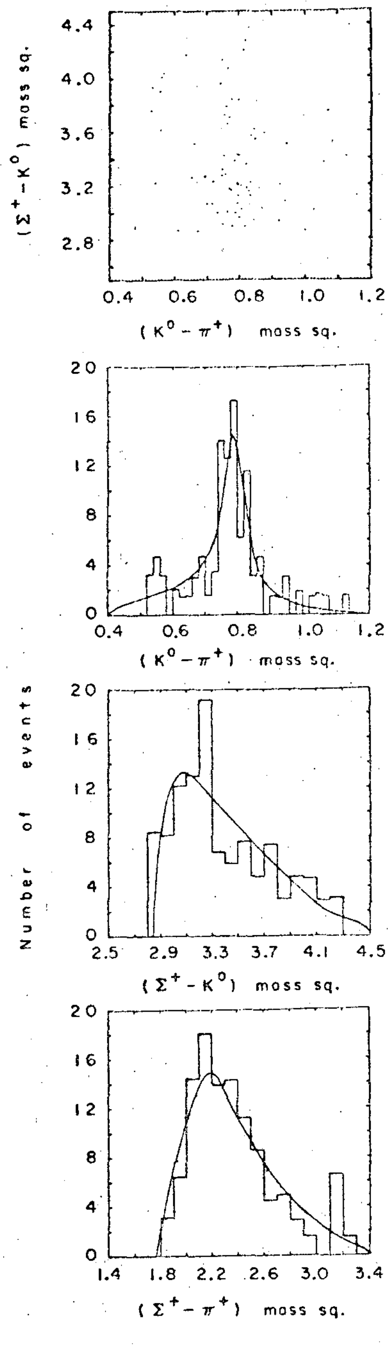
4.4
4.0
3.6
3.2
2.8
($\Sigma^+ - K^0$) mass sq.
0.4 0.6 0.8 1.0 1.2
($K^0 - \pi^+$) mass sq.
20
16
12
8
4
0
0.4 0.6 0.8 1.0 1.2
($K^0 - \pi^+$) mass sq.
Number of events
20
16
12
8
4
0
2.5 2.9 3.3 3.7 4.1 4.5
($\Sigma^+ - K^0$) mass sq.
20
16
12
8
4
0
1.4 1.8 2.2 2.6 3.0 3.4
($\Sigma^+ - \pi^+$) mass sq.
XBL697-3159

Fig 15

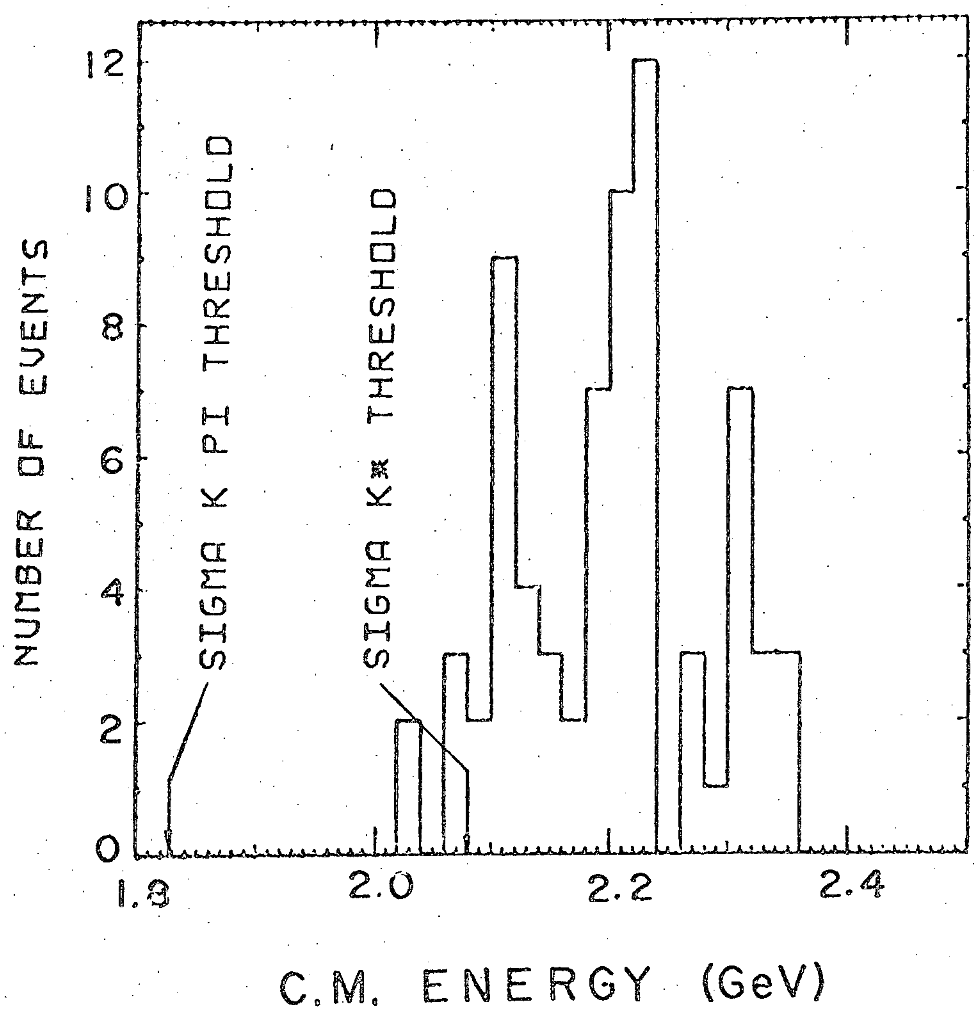

XBL 698-1103

Fig. 16

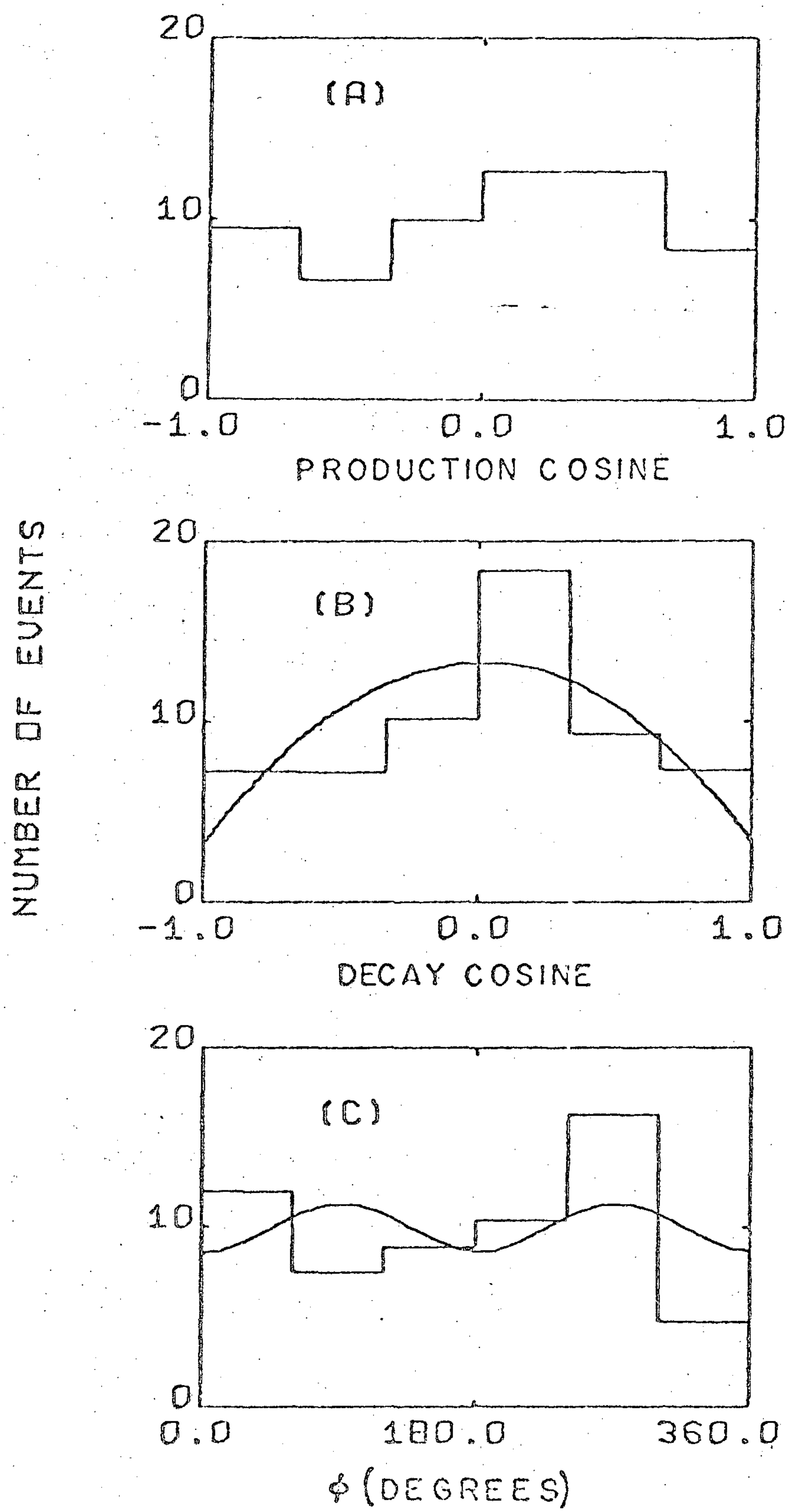

XBL 697-1060

Fig 17

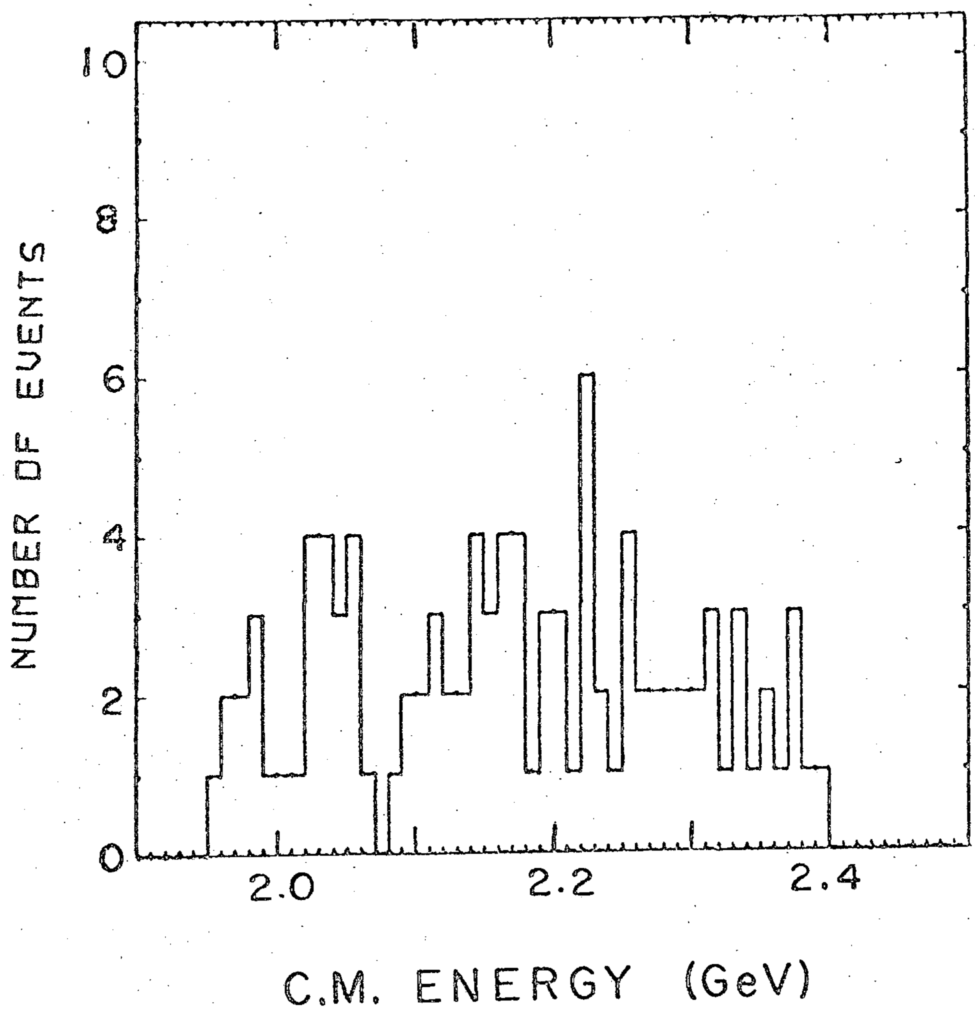

XBL 698-1102

Fig 18

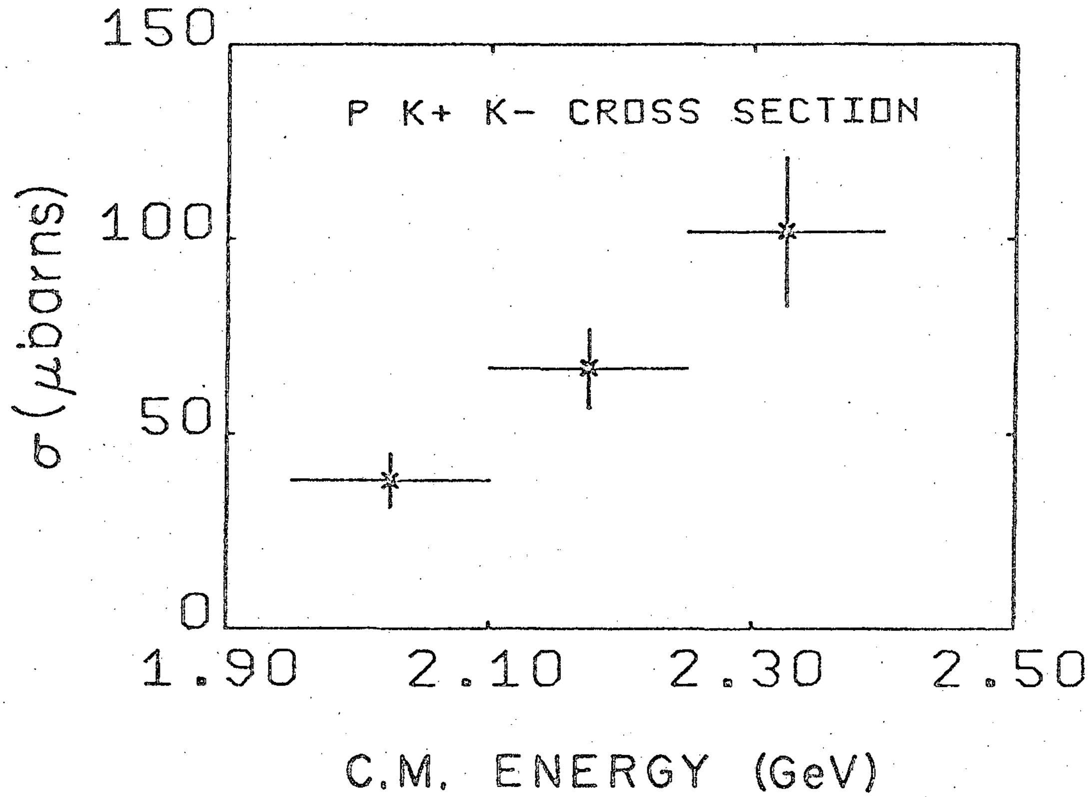

XBL 697-1061

Fig 19

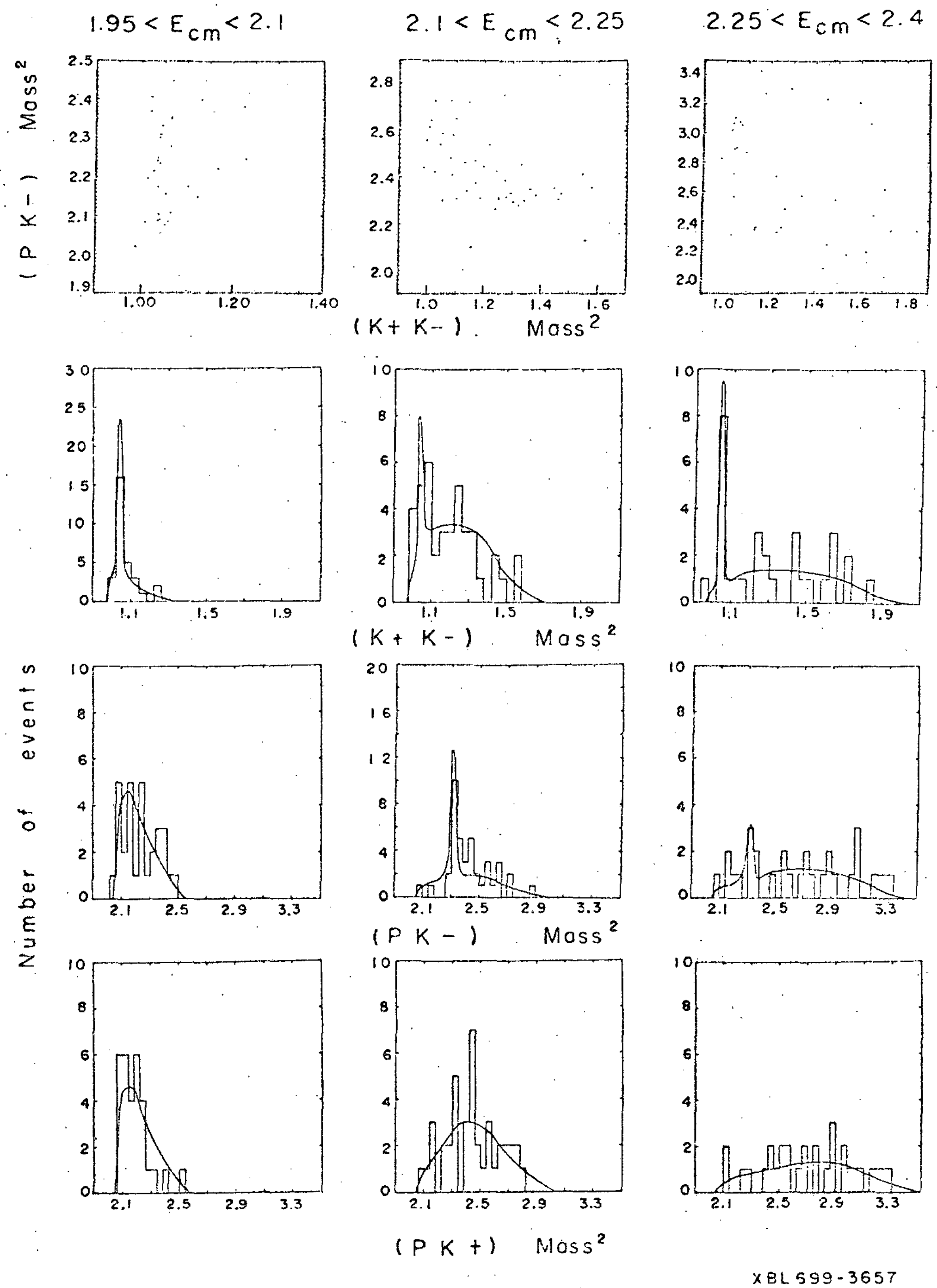

1.95 < E cm < 2.1
2.1 < E cm < 2.25
2.25 < E cm < 2.4
(P K-) Mass²
(K+ K-) Mass²
(K+ K-) Mass²
Number of events
(P K-) Mass²
(P K+) Mass²
XBL 699-3657

Fig 20

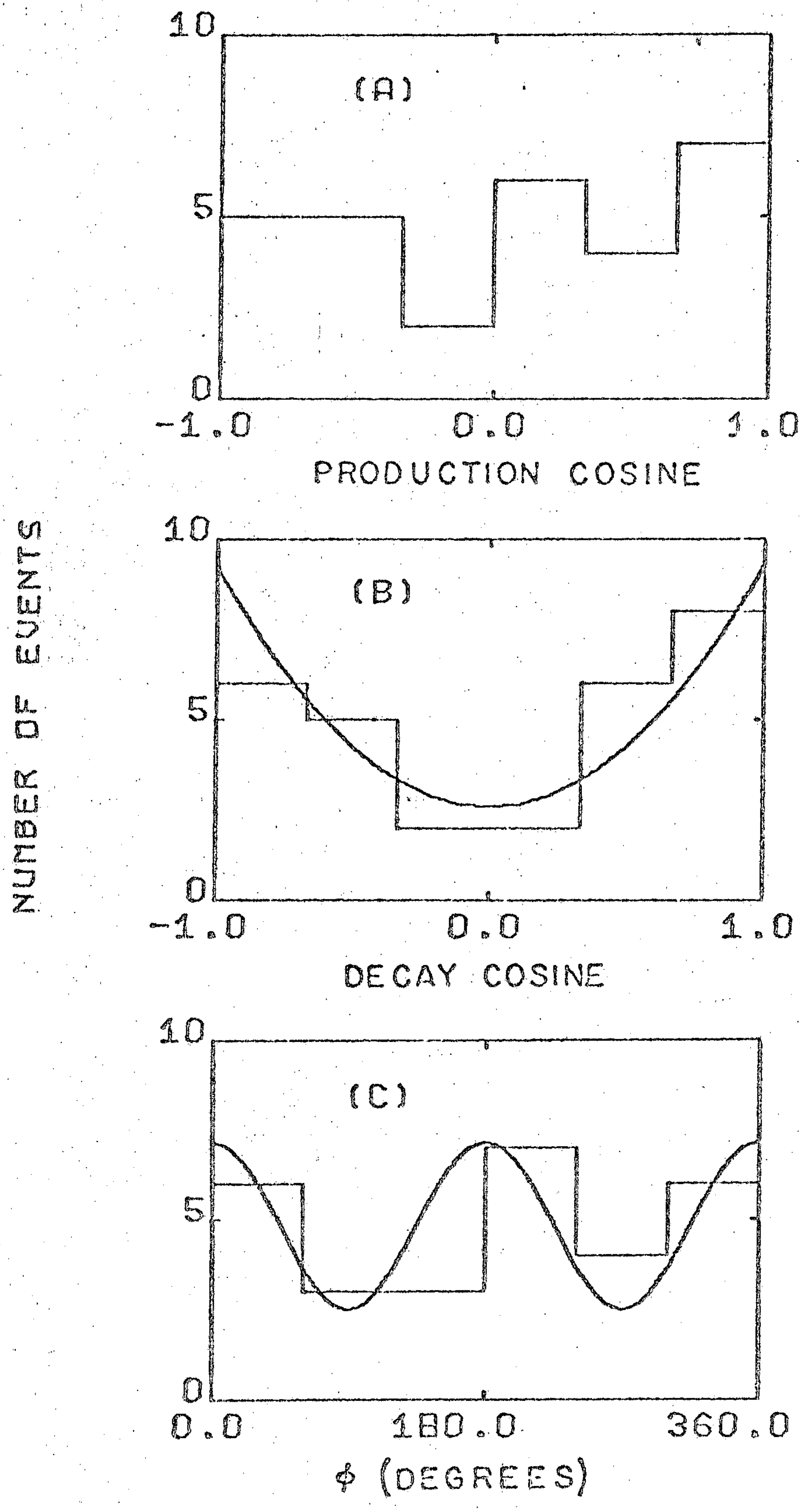

XBL 697-1062

Fig 21

TECHNICAL INFORMATION DIVISION
LAWRENCE RADIATION LABORATORY
UNIVERSITY OF CALIFORNIA
BERKELEY, CALIFORNIA 94720